

Multi-stage spontaneous symmetry breaking of light in Kerr ring resonators

Lewis Hill ^{1,2} , Gian-Luca Oppo ² & Pascal Del'Haye ^{1,3}

Symmetry breaking of light states is of interest for the understanding of nonlinear optics, photonic circuits, telecom applications and optical pulse generation. Here we demonstrate multi-stage symmetry breaking of the resonances of ring resonators with Kerr nonlinearity. This multi-stage symmetry breaking naturally occurs in a resonator with bidirectionally propagating light with orthogonal polarization components. The derived model used to theoretically describe the system shows that the four circulating field components can display full symmetry, full asymmetry, and multiple versions of partial symmetry, and are later shown to result in complex oscillatory dynamics - such as four-field self-switching, and unusual pulsing with extended delays between subsequent peaks. To highlight a few examples, our work has application in the development of photonic devices like isolators and circulators, logic gates, and random numbers generators, and could also be used for optical-sensors, e.g. by further enhancing the Sagnac effect.

¹Max Planck Institute for the Science of Light, Staudtstraße 2, D-91058 Erlangen, Germany. ²Department of Physics, University of Strathclyde, 107 Rottenrow, Glasgow G4 0NG, UK. ³Department of Physics, Friedrich Alexander University Erlangen-Nuremberg, 91058 Erlangen, Germany. ✉email: lewis.hill@mpl.mpg.de

Spontaneous symmetry breaking (SSB) phenomena are of fundamental importance to many areas of science with some notable examples being the Brought-Engler-Higgs mechanism in particle physics¹, the superconductivity of metals in condensed-matter physics, early universe models², plasmonics³, and even the evolution of swimming and flying organisms in fluid dynamics and biology^{4,5}. In the field of non-linear optics, there has been a recent explosion of work studying SSB in Kerr ring resonators.

A Kerr ring resonator is a closed loop optical path, made of a Kerr material where the refractive index depends on the intensity of a strongly interacting coherent (laser) field. Laser light enters and leaves the looped path of the resonator through optical couplers such as beam splitters or evanescent coupling, in setups similar to that displayed in Fig. 1. The cavity fields evolve as they circulate the resonator due to a combination of the input pump powers, laser detunings, interactions with the Kerr material, and losses. Depending on the transmission of the two-way coupler, the fields can circulate within the resonator for a very large number of round trips, allowing for long evolution times. Upon leaving the resonator, via the coupling mechanism, the circulating fields then progress on towards different outputs where they can be further processed or measured. Note however that Fig. 1 shows a more complex scenario than a typical single input Kerr resonator, in that two counter-propagating laser inputs are used rather than a single one. These two inputs are subsequently split into different orthogonal polarisation components. This configuration is the device of reference for the work presented here.

To date, studies of SSB in Kerr ring resonators have focused on single-stage phenomena, where, for example, a symmetric property is broken via a single bifurcation into a limited two asymmetric states, such as two symmetric resonance frequencies splitting into two that are then unequal. Symmetry breaking phenomena involving multiple bifurcations (referred here as multi-stage), where a symmetric property subsequently breaks into more than two asymmetric states, which are common in,

for example, biology⁵, have however so far remained unreported.

Common example mechanisms for observing single-stage SSB in Kerr ring resonators use counter-propagating fields or use two orthogonally polarised, co-propagating, field components. In the first example, two, otherwise identical, input beams enter the resonator in opposite directions. The evolutions of these fields, including their SSB, have been studied extensively theoretically^{6–13}, and, more recently, experimentally^{14–18}. The second example involves a single, linearly polarised, laser input splitting into two orthogonally polarised components. Theoretically this SSB was investigated by Geddes et al.¹⁹ when considering transverse diffraction via two coupled Lugiato-Lefever equations²⁰, and in by ref. ²¹ when considering longitudinal dispersion via two driven and damped nonlinear Schrödinger equations. This two-polarization setup, and its SSB, have also seen a recent flurry of studies, both theoretical and experimental^{9,10,22–26}.

In order to achieve the elusive multi-stage SSB, we investigate here if this would occur via the combination of the above two well-known mechanisms. It is this combined system that is displayed in Fig. 1 and forms the basis of our analysis.

Motivation for the attainment of multi-stage SSB in ring resonators, beyond fundamental curiosity, lies in the myriad successes of the single-stage systems. The polarisation system can be used for example as a polarization controller²³ and for producing SSB temporal cavity solitons²⁴ and breathers²⁵ with the potential to provide novel methods for two-components frequency combs. While the counter-propagating system, on the other hand, can be used to enhance the Sagnac effect⁶ for the development of rotation sensors with increased sensitivity, and to realise isolators and circulators²⁷ for, for example, all optical computing.

Our aim here, therefore, is to derive and deliver a robust theoretical framework to guide the experimental realisation of a system that proves itself capable of greatly expanding the range of

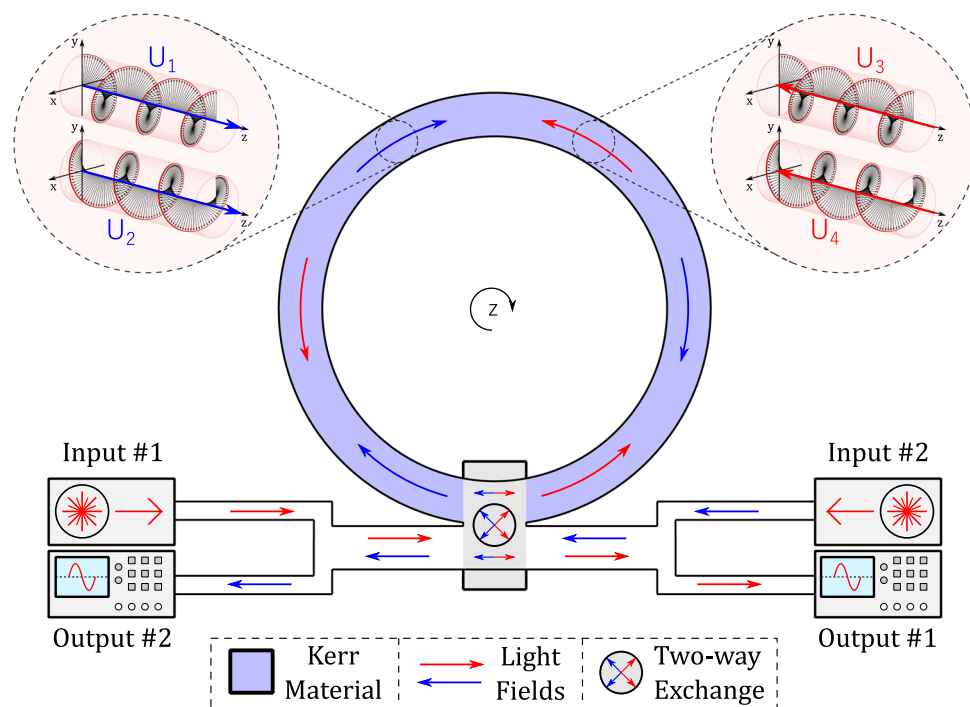


Fig. 1 Studied setup. Two identical, linearly polarised, laser inputs enter a Kerr ring resonator (shaded blue) via a two-way coupling mechanism from opposing directions. This leads to two counter-propagating, linearly polarised, fields circulating the resonator, red and blue coloured arrows respectively. By splitting the linearly polarised light fields into left- and right-circularly polarised components we obtain a total of four circulating fields, U_{1-4} .

ring resonator applications in general, while also providing a potential route for replacing multiple resonator devices with a single one.

Results and discussions

This section describes results from using the system of equations described, and derived, in the methods section of this paper, which model the four circulating components $U_{1\rightarrow 4}$ of Fig. 1.

Multi-stage and multi-regional SSB. Figure 2 shows the evolutions of the intensities of the four circulating components, $|U_{1\rightarrow 4}|^2$, during an input intensity, $|E_{in}|^2$, scan for a select cavity detuning value of $\theta = 3.85$. This figure was created by numerically integrating Eqs. (4). The solid lines of the scan show the natural evolution of the circulating field intensities as the input power is gradually decreased. It can be seen that for the lower input power values of this scan the single solid line (blue) mimics analogous results of the separate models described in the introduction; that is to say that for very low input intensities all four fields have fully-symmetric, or equal, intensities: $|U_1|^2 = |U_2|^2 = |U_3|^2 = |U_4|^2$. At higher values of the input intensity however, beginning at around $|E_{in}|^2 = 0.82$ in this example, one observes that this single solid line bifurcates into two (cyan) solid lines, and itself becomes a dashed line (indicating here an unstable solution). This bifurcation is indicative of spontaneous symmetry breaking, where now, rather than full symmetry between the circulating field intensities the four fields separate into two stable asymmetric pairs of symmetric fields, with those pairings being either $|U_1|^2 = |U_2|^2 \neq |U_3|^2 = |U_4|^2$ or $|U_1|^2 = |U_3|^2 \neq |U_2|^2 = |U_4|^2$. This pair-separation amounts to either a propagation direction or circular-polarization symmetry breaking respectively, with the type of SSB and the dominant and submissive roles taken by the two asymmetric pairs both being randomly assigned by the noise within the system. This bifurcation

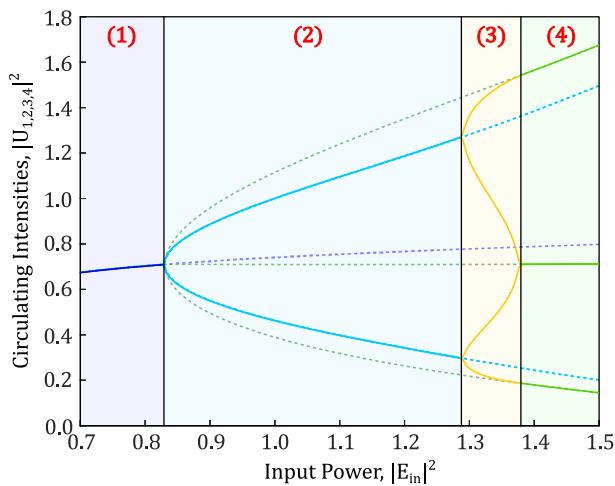


Fig. 2 An input power scan of Eq. (4) for detuning $\theta = 3.85$. The scan runs from right to left with the previous end iteration used as the initial condition for the next input value. The solid lines show the natural circulating evolutions, with indicative shading, while the dashed lines show unstable states. Note that the solid line has four distinct regions with shaded backgrounds. Region (1) has full symmetry where all fields have equal intensity; region (2) begins with a symmetry breaking pitchfork bifurcation and results in two asymmetric pairs of symmetric fields; region (3) begins with a second symmetry breaking pitchfork bifurcation, leading to four entirely asymmetric fields, and finally region (4) begins with a partial-symmetry restoring pitchfork bifurcation, leading to a single pair of symmetric fields, with the remaining two fields being both asymmetric to each other and to the symmetric pair.

will likely come with little surprise to those knowing the theory of the separate systems since it represents the well-known single-stage symmetry breaking.

Atop the solid (stable) cyan lines, and the dashed blue line, in this region there are other possible solutions, displayed by dashed green lines. This type of, currently unstable, solution later becomes stable, and will be discussed then. Note that the dashed lines of Fig. 2, which show stationary but unstable states of the system, are still discoverable by numerical integration when we forcibly set, for example, $U_1 = U_2 = U_3 = U_4$ (blue), $(U_1 = U_2) \neq (U_3 = U_4)$ (cyan), and $U_1 = U_4$ (green).

Tracking the input intensity to higher still values one sees a secondary bifurcation, where the previously stable cyan line splits into two stable yellow lines while becoming itself unstable. This should immediately be recognised as a nested SSB bifurcation, resulting in full asymmetry between the circulating field intensities: $|U_1|^2 \neq |U_2|^2 \neq |U_3|^2 \neq |U_4|^2$. Through this scan we have thus observed a fully symmetric state break into asymmetric pairs and finally then break again into a full asymmetric state i.e. we have just observed the sought multi-stage spontaneous symmetry breaking.

Pausing, momentarily, to reflect upon the implications of this result. Firstly, as is explained by Kaplan et al.⁶, one can enhance the Sagnac effect through exploiting the SSB of counter-propagating fields. Since the degree of enhancement is proportional to the magnitude of the difference between the circulating components, we can actually enhance the Sagnac effect further still through our multi-stage SSB. This is since we see that the fully asymmetric solutions of our system allow for a greater difference between the most dominant and most submissive field components, than that which exists for the single-stage break. This therefore has the potential to develop hyper-sensitive rotation sensors. Secondly, the wider diversity of possible system states, and the freedom to manipulate the resonator through said states, lends itself to the possible development of logic gates, building upon methods previously proposed using single-stage SSB²⁸, capable of more complex operation. Similarly, the multi-stage structure allows for the development of polarisation dependent isolators and circulators²⁷. Finally, we immediately recognise the possibility of multi-stage SSB phenomena perhaps doubling, or more, the rate at which random numbers may be generated based upon recently proposed single-stage SSB techniques²⁹.

Returning attention to Fig. 2, we note, at last, the surprising “partially”-symmetric region, caused by a solo symmetry restoring bifurcation in but two of the components alone. In this region, the previously unstable (dashed green line) solutions becomes stable (solid green). This line describes a single symmetric pair of field components, with the remaining two left asymmetric both to each other and to the symmetric pair. I.e. $|U_i|^2 \neq |U_j|^2 = |U_k|^2 \neq |U_l|^2 \neq |U_i|^2 \neq |U_l|^2$, where here the solo symmetric pair can be with $|U_1|^2 = |U_4|^2$ or $|U_2|^2 = |U_3|^2$. This indicates a symmetry retention along one of the diagonals of Table 1 with asymmetry between the remaining diagonal elements of the table. A region that also lends itself to many of the applications above.

In summary, we find four system states in relation to various degrees of symmetry within the system: (1) full symmetry, (2) two symmetric pairs, (3) full asymmetry, and (4) one symmetric pair with the others asymmetric.

To gain a better understanding of the useful states of Eqs. (4), we display in Fig. 3 the results of numerical scans in the parameter space of input power $\ln(|E_{in}|^2 + 1)$ and cavity detuning θ , with the various field intensity relations described in the figure caption. The detuning range of this figure is from 0 to 5.5, while a

Table 1 Transformations to circular polarisation basis.

	Clockwise propagating	Counterclockwise propagating
Left Circ. Polarised	$U_1 = \frac{\epsilon_{\text{cwk}} + i\epsilon_{\text{cwy}}}{\sqrt{2}}$	$U_3 = \frac{\epsilon_{\text{ccwk}} + i\epsilon_{\text{ccwy}}}{\sqrt{2}}$
Right Circ. Polarised	$U_2 = \frac{\epsilon_{\text{cwk}} - i\epsilon_{\text{cwy}}}{\sqrt{2}}$	$U_4 = \frac{\epsilon_{\text{ccwk}} - i\epsilon_{\text{ccwy}}}{\sqrt{2}}$

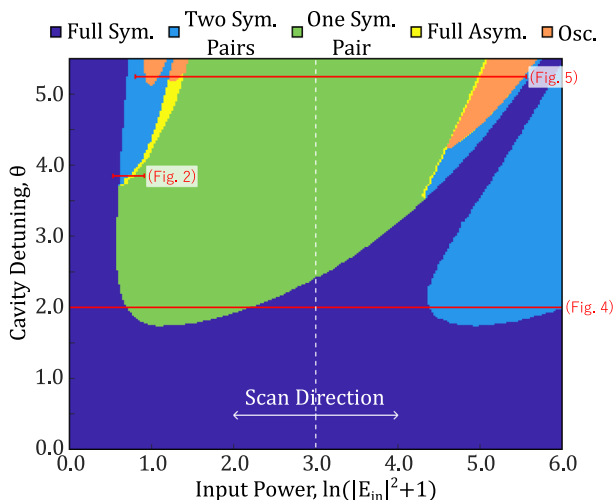


Fig. 3 Input power–cavity detuning parameter space. The dark blue region corresponds to fully symmetric stable solutions, the light blue region to two asymmetric pairs of symmetric fields, the green region to a single pair of symmetric fields, with the remaining two fields being both asymmetric to each other and to the symmetric pair, and finally the yellow region corresponds to four fully asymmetric fields. Also included is an orange overlay which indicates the regions where the fields are unstable to temporal oscillations. Red lines indicate the slices of the scan shown in Figs. 2, 4 and 5 respectively.

similarly normalized detuning of up to 15 has been achieved experimentally by ref. 24. Similarly, input powers of up to $|E_{in}|^2 = 11.5$ have also been used experimentally, again by ref. 24, while many results here require only up to $|E_{in}|^2 = 3.5$. We further believe that the experimental realisation of normalised input powers beyond this referenced experimental value is realistic. This is owed to their dependencies on resonator design properties, such as resonator finesse, length, and Kerr response. It can be seen that the system’s dynamics are very rich, and that specific relationships between field intensities, such as being fully asymmetric, are highly dependent on the input parameters. In this scan we see additional regions of special interest, such as the isolated second SSB, light blue, region, which emerges on the right-hand side of the plot, and the orange regions, indicating the temporal oscillations that emerge at high detuning values.

First focusing on the interest of the second isolated SSB region, we provide an input intensity scan for $\theta = 2$ in Fig. 4. Here we show, again with solid lines, the natural evolution of the circulating fields as we decrease the input power. Also shown with dashed lines, are the stationary but unstable solutions when we force $U_1 = U_2 = U_3 = U_4$ (dashed blue) and $U_1 = U_2, U_3 = U_4$ (dashed cyan). We see that at input powers of region (4) the states with a single symmetric pair (green) are stable at the expense of the state with two asymmetric symmetric-pairs (cyan). We further note that the most and least intense field components of the green solution set in this region are always higher than those for the blue solution set, meaning that this region can also be used

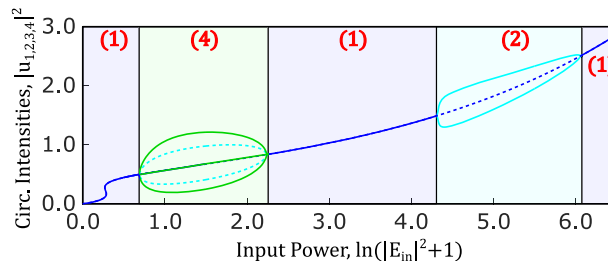


Fig. 4 Input intensity scan of Eqs. (4) for detuning $\theta = 2$. For this low detuning value we provide a much larger range of input intensity values than in Fig. 2. This is to highlight a second symmetry broken region which emerges at high input intensity values (light blue region on the RHS of Fig. 3).

to further enhance the Sagnac effect by the method based upon intensity difference as described by refs. 6,7. Comparing the differences between the most and least intense field components for an example selected input power of $\ln(|E_{in}|^2 + 1) = 1.4$, we find a 70% increase in the difference when comparing the multistage symmetry broken solution set (green) to the single stage (cyan). Further, perhaps quite surprising to those who study the separate system, one may also see the second, entirely separate, symmetry broken regime which emerges at high input intensities. Within this region lies the previously unstable asymmetric symmetric-pairs of fields. That is to say, in this high input intensity region the pairings $|U_1|^2 = |U_4|^2$ & $|U_2|^2 = |U_3|^2$ are stable, with the other possible combinations of pairings previously described now being unstable. This means that within our system any combination of two asymmetric symmetric-pairs are stable and observable at some point in parameter space.

Temporal oscillations, chaotic attractors, and spontaneous switching. As hinted at by the orange overlay on Fig. 3, the system described by Eqs. (4) is susceptible to oscillations for some parameter regions. In Fig. 5 we display the full range of possible oscillatory behaviours for a selected value of the detuning $\theta = 5.25$. In subsequent figures we display these behavioural regions in more detail.

Focusing first on the LHS of Fig. 5, in Fig. 6 we present the temporal evolutions of the intensities of the four fields and in the corresponding complex planes after transients have been discarded for $\theta = 5.25$, and $\ln(|E_{in}|^2 + 1) = 1.0$, panels (a) and (b), $\ln(|E_{in}|^2 + 1) = 1.25$, panels (c) & (d). The examples provided in Fig. 6 are characteristic of the two orange regions on the far left of Fig. 3, respectively, and show that these regions are quite different in nature. The first region displays oscillations where the four fields have split into two asymmetric symmetric-pairs, as described in the above section, (see Fig. 6a, b), whereas in the second region all four fields oscillate in a fully asymmetric way with respect to one another (see Fig. 6c, d).

Turning attention to the RHS of Fig. 5, we now focus on the the range of field intensity oscillations for high input intensities. We show, in Fig. 7, the distinct types of oscillations which are possible here. The first type of oscillation occurs when two asymmetric symmetric-pairs of fields, again with the possible combinations of fields described in the above section, follow the same phase-space paths and have the same average intensities (see red lines of Fig. 5). An example of this type of behaviour is displayed in Fig. 7a, b, for input intensity $\ln(|E_{in}|^2 + 1) = 5.5$. Due to the overlap of the phase space paths and the average intensities, this type of oscillation is very similar to those shown in Fig. 6a, b, which leads to this state retaining some of its underlying symmetry. We note, however, that unlike Fig. 6a, b the fields here do not oscillate in phase and all four fields have fully

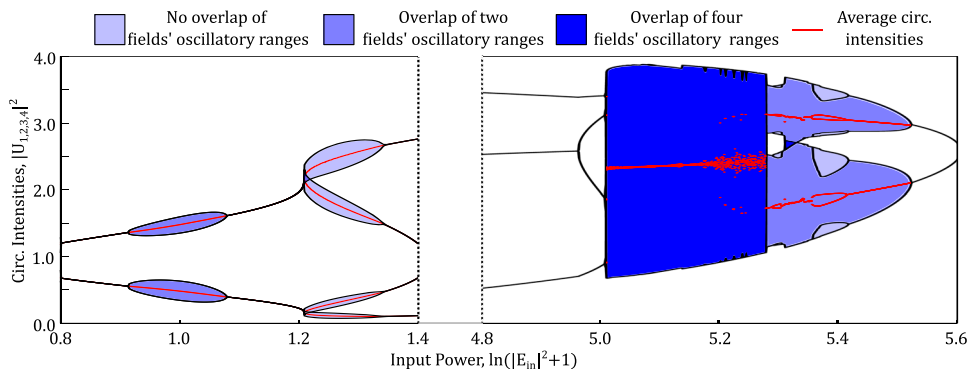


Fig. 5 Field oscillation intensity ranges against input intensity for detuning $\theta = 5.25$. The solid black lines of the plot trace the maxima and minima of the four field’s oscillatory ranges for the given input intensities (meaning up to eight black lines for some input intensities are possible). Regions shaded in different tones of blue indicate where oscillations are occurring. The tone of the blue shading itself indicates how many different fields overlap in their respective oscillation intensity ranges. The lightest blue indicates no overlap between any number of fields, the darkest shading implying all four field’s oscillatory ranges overlap in this region, and finally the intermediate tone implies that only two of the four field’s oscillatory ranges overlap in this region. The red lines track the averages of the four fields over many oscillations, four red lines are always present but may overlap where fields have globally symmetric intensity evolutions.

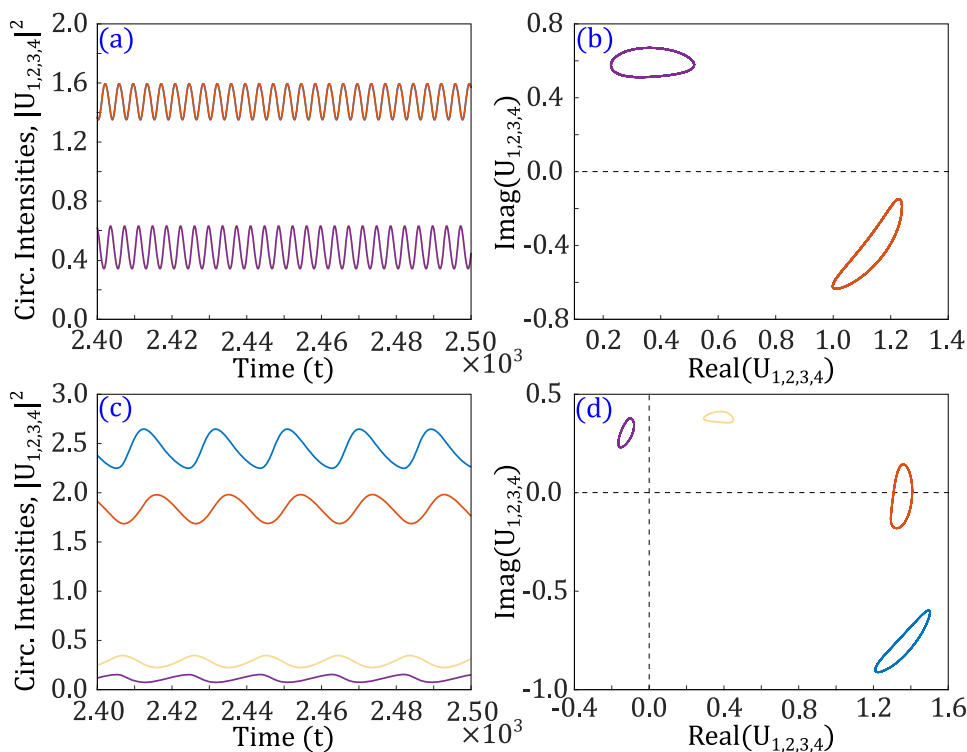


Fig. 6 Field intensity evolutions and their complex phase-space paths. For detuning $\theta = 5.25$ and input powers $\ln(|E_{in}|^2 + 1) = 1.0$, for (a, b), and $\ln(|E_{in}|^2 + 1) = 1.25$ for (c, d), we show the field intensity evolutions over time, (a, c), and their complex phase-space paths, (b, d). Each of the four coloured lines corresponds to one of the four circulating fields $U_{1 \rightarrow 4}$. Computed by integrating Eqs. (4). Note that in (a, b) two pairs of fields evolve together causing two pairs of exact line overlaps, where as in (c, d) all four fields evolve asymmetrically to each other resulting in four distinct lines in each panel.

asymmetric intensity evolutions. This type of behaviour provides an alternative way to obtain self-switching between dominant and suppressed fields in polarisation or counter-propagating systems, as discussed by refs. ^{11,12}. In these studies the “periodic self-switching”-regions were extremely narrow, while here we observe very broad regions where periodic self-switching behaviour is possible.

In Fig. 5, one observes a pale-blue region around $\ln(|E_{in}|^2 + 1) = 5.4$ beginning and ending with bifurcations in both the black (tracking the minima and maxima of the field intensity oscillations) and red (tracking the average of the field intensity oscillations) lines.

These bifurcations beginning and ending the region are known as global symmetry breaking and global symmetry restoring bifurcations respectively, and correspond to a single symmetric attractor splitting into two attractors and to two attractors being the symmetric of each other and merging. In either case, the global bifurcations produce sudden and large changes to the morphology of the attractors and can be identified by the merging of attractor paths in the complex phase space. The types of oscillations which occur within these regions are characterised by the example oscillation traces shown in Fig. 7c, d, where $\ln(|E_{in}|^2 + 1) = 5.4$. Note that the previous pairs of fields which held residual

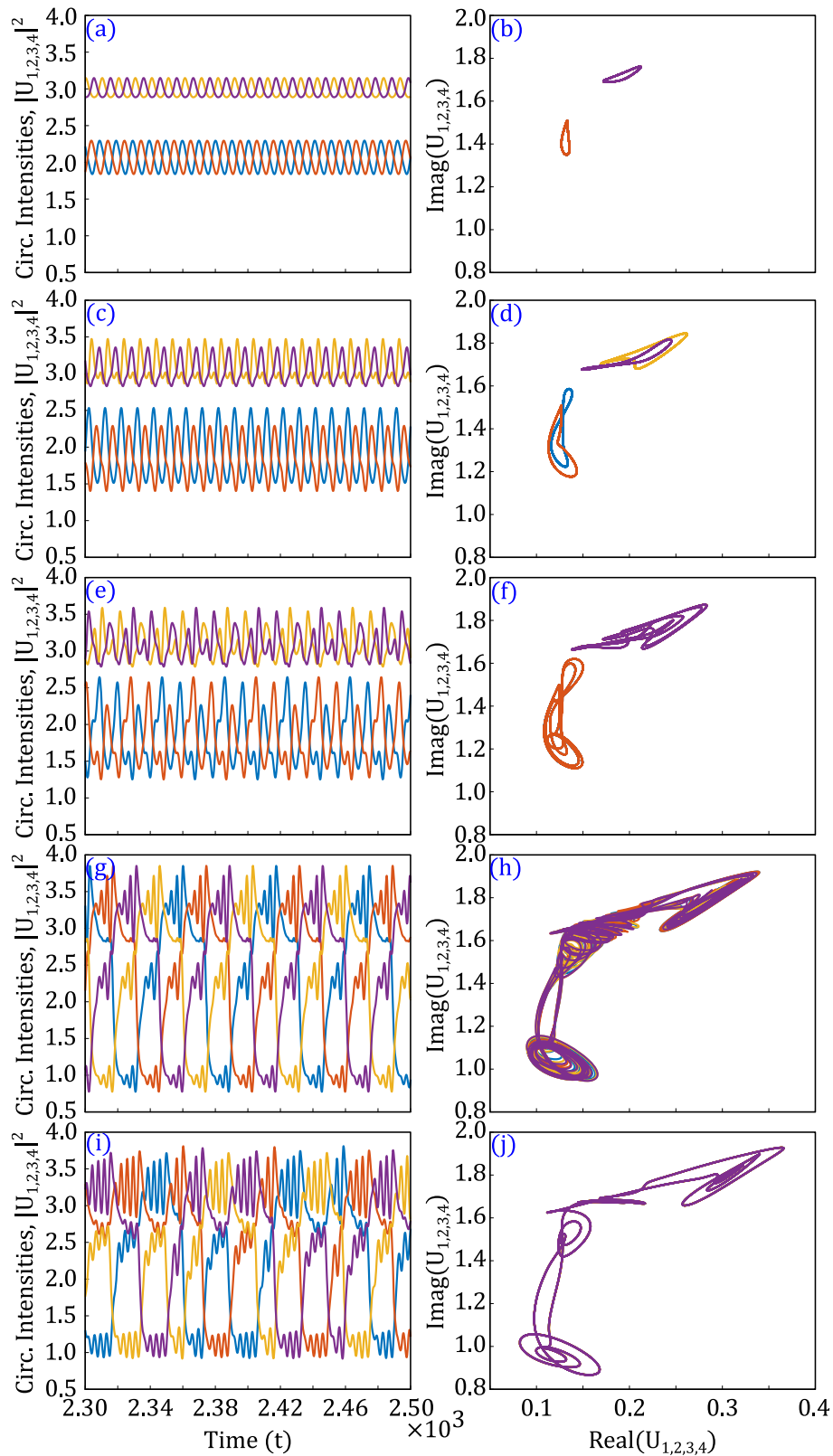


Fig. 7 Field intensity evolutions over time and their complex phase-space paths. The oscillations are for $\theta = 5.25$, (**a, b**): $\ln(|E_m|^2 + 1) = 5.5$, (**c, d**): $\ln(|E_m|^2 + 1) = 5.4$, (**e, f**): $\ln(|E_m|^2 + 1) = 5.3525$, (**g, h**): $\ln(|E_m|^2 + 1) = 5.2$, and (**i, j**): $\ln(|E_m|^2 + 1) = 5.1$, computed by numerically integrating Eqs. (4). (**a, c, e, g, i**) show the intensity evolution; (**b, d, f, h, j**) show the complex phase. For more detailed discussion please refer to main text.

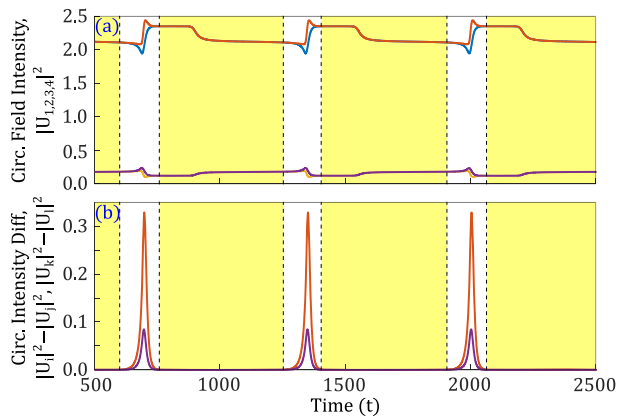


Fig. 8 Pulsing dynamics. By taking the difference between the intensities of the two fields existing in close pairs (a) as they evolve over time, pulse structures (b) can be observed with long delays between their production. The example displayed is for an input laser intensity of $\ln(|E_{in}|^2 + 1) \approx 1.21$ and detuning $\theta = 5.25$.

average-intensity symmetry have split, and their complex-phase-space attractors have also split into two separate attractors—indicating a global symmetry breaking bifurcation. Ending these regions however, the average-intensity and complex-phase-space path symmetries are restored, and the split attractors merge once again (a global symmetry restoring bifurcation), with an example of this shown in Fig. 7e, f where $\ln(|E_{in}|^2 + 1) = 5.35$.

There are also extended regions of non-periodic switching, Fig. 7g, h, and later even four-field periodic switching. This is seen where a single continuous red line is displayed in Fig. 5, where all attractors have merged perfectly, resulting in all four fields displaying symmetric average intensities and perfectly overlaid phase-paths, Fig. 7i, j.

Slowtime pulsing behaviour. To complete our discussions surrounding the system's temporal dynamics, we display pulsing behavior on the slow time scale with long delays between each structure generation. This occurs within the region where all four fields can oscillate with separate values of their intensities as one approaches the region's low-input-intensity limit—at approximately $\ln(|E_{in}|^2 + 1) = 1.21$ in Fig. 5. An example of this is shown in Fig. 8. The pulse structures can be observed by taking the difference between two of the circulating fields, as shown in Fig. 8b, with possible pairings of the top two and bottom two fields being $|U_1|^2 = |U_2|^2$ & $|U_3|^2 = |U_4|^2$ or $|U_1|^2 = |U_3|^2$ & $|U_2|^2 = |U_4|^2$. These structures are a result of the system periodically almost gaining and then rapidly losing either of the polarization or propagation-direction symmetries in this region via a relaxational limit cycle.

Focusing on only, for example, the top two fields of Fig. 8, in Fig. 9b we show our theorised HSS. It contains an optical bistability cycle of the symmetric state, say $|U_1|^2 = |U_2|^2$, coexisting with asymmetric solutions, all of which are unstable to oscillations. The observed intensity evolutions of Fig. 8a can then be explained by the following consideration: focusing on one period of the intensity oscillation in Fig. 9a, the two fields begin with almost perfect polarization or propagation-direction symmetry on the lower branch of the optical bistability of Fig. 9b, purple dot. This HSS is metastable so that the system initially evolves away from this symmetric point and is attracted to the two asymmetric solutions, blue and red dots respectively of panel (b), leading to an increasingly large asymmetry between, as an example, the intensities of the two polarization components of the field. Since we predict the asymmetric HSS to be unstable to

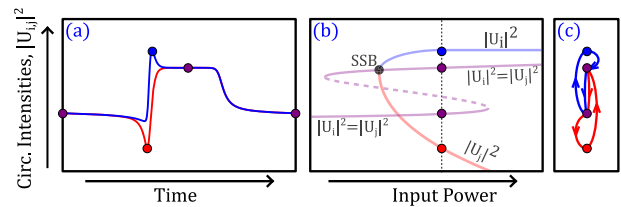


Fig. 9 Relaxational limit cycle. a Intensity evolutions which can cause pulse structures when subtracted. b Theorised HSS diagram explaining the field dynamics producing (a). c Visual representation of how the fields oscillate between the various HSS that we theorise are possible in (b).

oscillations however, the system does not settle on the asymmetric values, and instead it is drawn to a predicted attractive but metastable symmetric solution which lies on the upper branch of the symmetric optical bistability. Unable to find a stable solution even here however, the system continues to oscillate where it is attracted to the original symmetric, but metastable, solution on the lower branch of the HSS, and the cycle then repeats. This process is summarised in panel (c) with arrowed paths.

The proposed explanation in terms of metastable states on an optical bistable cycle and unstable asymmetric branches is further supported by similar observations in the separate systems⁷, supplemented with the, required, nested spontaneous symmetry breaking bifurcations—the primary result of this paper.

Conclusions

We derived and presented a theoretical model for Kerr ring resonators with two counter-propagating input beams with two orthogonally polarized components for each beam. The model predicts that the physical system will be able to display a vast number of novel behaviours while simultaneously also being able to mimic simpler systems if required.

We showed that the system is capable of multi-stage symmetry breaking bifurcations and restoring events; capable of displaying full symmetry, partial-symmetry breaking and restoring, and even total asymmetry. These results alone allow for, for example, hyper-enhancement of the Sagnac effect, complex logic gates, polarization-dependent isolators and circulators, and efficient random number generation.

Turning attention to the stability of the system and its susceptibility to oscillations, we completed a behavioural scan of the system for a range of parameters, which revealed a number of regions where the system was unstable and susceptible to a range of oscillatory behaviours—again with various degrees of symmetry broken or retained. We showed that multiple chaotic attractors can merge as input parameters are varied, and that this leads to not only two-field self-switching but also the complex dynamical behaviour of four-field self-switching, brought about by a global symmetry restoring bifurcation. Contrary to the self-switching dynamics of the separate systems, which occurred for only small windows of input parameters, our self-switching dynamics were shown to be maintained for large input ranges.

Atop these novel field behaviours, the system further provides the option of producing, on a *single* device, the field behaviours of the two separate systems, counter-propagation and orthogonal polarizations. This is to say, it can produce the behaviours of two counter propagating fields—lending itself to applications such as enhancing the Sagnac effect for use in rotation sensors⁶, gyroscopes¹⁶, and elsewhere, and in the realisation of all-optical components, such as isolators and circulators²⁷, while also being able to produce the behaviours of the system with two orthogonal polarisation components, allowing for applications such as acting as a Kerr polarisation controller²³, potentially supporting

(fast-time) temporal cavity solitons for the generation of frequency combs^{24,25}, or for use in optical neural networks used in artificial intelligence applications or for systems for quantum information processing³⁰. The benefit of this combined system however should be obvious—it can achieve the behaviours of both systems simultaneously, all while taking place within one resonator. For industrial applications this has the benefit of saving both space and fabrication costs, and should be easily achievable with current resonator or fibre loop technology. There would also be applications of the physical system in high speed telecommunication systems, particularly for polarization mode multiplexing and for the possibility of having counter-propagating light in telecoms systems. For these reasons, physical realisation of these devices can benefit from the wide range of predicted behaviours displayed here.

Methods

We first derived a mathematical model to aptly describe the system of Fig. 1. As indicated by our introduction, this system is comprised of two counter-propagating, linearly polarised, laser inputs, which enter a Kerr ring resonator via optical couplers (e.g. a waveguide close to the resonator). The circulating light fields within the resonator can then be decomposed into orthogonal polarization components, as shown in Fig. 1. As a starting position for our model, we first consider the propagation of a single vectorial field, E , in a Kerr ring cavity as discussed in by ref.¹⁹. When normalized and neglecting dispersion or diffraction, one obtains:

$$\frac{dE}{dt} = E_0 - (1 + i\eta\theta)E + i\eta[A(E \cdot E^*)E + B(E \cdot E)E^*], \quad (1)$$

where $E = \mathcal{E}_x\hat{x} + \mathcal{E}_y\hat{y}$ is the normalised vector electric field envelope (comprised of components along the x and y axis respectively, with the cavity axis along z), E_0 is the input field, $\eta = \pm 1$ in the case of a self-focusing and self-defocusing medium respectively, θ is the cavity detuning (the difference between the input laser frequency and the closest cavity resonant frequency) and the constants A, B represent the self- and cross-phase modulation strengths respectively¹⁰, which are here given by:

$$A = \left(\chi_{1122}^{(3)} + \chi_{1212}^{(3)} \right), \quad B = \chi_{1221}^{(3)}, \quad (2)$$

where $\chi^{(3)}$ is the third order susceptibility tensor³¹.

The self- and cross-phase modulation constants describe the strengths with which the two polarisation components affect themselves and each other, respectively, as they circulate the ring resonator¹⁰.

We next sought to generalise this model to take into account an additional input of Fig. 1, which causes a second, counter-propagating, field to circulate within the resonator. We did this by considering the propagation of light in the medium in a manner similar to that outlined by ref.³², that is, we set clockwise, subindex cw , and counter-clockwise, subindex ccw , polarization components via:

$$\mathcal{E}_{x,y} = \mathcal{E}_{cw,x,cwy}e^{ikz} + \mathcal{E}_{ccw,x,ccwy}e^{-ikz}, \quad (3)$$

where k the light wavevector. By expanding Eq. (1) with Eq. (3), neglecting the fast varying terms, and separating all $\mathcal{E}_{cw,x}$, $\mathcal{E}_{cw,y}$, $\mathcal{E}_{ccw,x}$, $\mathcal{E}_{ccw,y}$ terms as far as possible, one eventually arrives at a relatively long system of four coupled equations. We then simplified these equations by moving to a circular polarisation basis as defined in Table 1.

In this basis our model takes on the more succinct form of Eqs. (4), where E_{in} is the input amplitude E_0 in this new basis and $C = A + 2B$. Similar to Eq. (1), the first terms within the square brackets of Eqs. (4) are caused by self-phase modulation, whereas the second, third, and fourth terms are caused by cross-phase modulation. The last term is responsible for an energy exchange between the two circular components of each beam³², an exchange which is not present in the separate models. This final component also prevents us from finding the homogeneous stationary states (HSS) of the system in the usual manner¹⁰, although we can still numerically integrate Eqs. (4) using well-known Runge–Kutta techniques to search for stable or dynamic solutions.

For equal pumping and detunings, Eqs. (4) is invariant under the transformations that exchange the indexes 1 with 2 and 3 with 4 (polarization component exchange), that exchange the indexes 1 with 3 and 2 with 4 (line counter-propagation component exchange) and that exchange the indexes 1 with 4 and 2 with 3 (cross counterpropagation component exchange). These are the various

symmetries that are broken by bifurcations we describe.

$$\begin{aligned} \frac{dU_1}{dt} &= E_{in} - (1 + i\eta\theta)U_1 + i\eta[(A|U_1|^2 + C|U_2|^2 + 2A|U_3|^2 + C|U_4|^2)U_1 + CU_3U_4^*U_2], \\ \frac{dU_2}{dt} &= E_{in} - (1 + i\eta\theta)U_2 + i\eta[(A|U_2|^2 + C|U_3|^2 + 2A|U_4|^2 + C|U_1|^2)U_2 + CU_4^*U_3U_1], \\ \frac{dU_3}{dt} &= E_{in} - (1 + i\eta\theta)U_3 + i\eta[(A|U_3|^2 + C|U_4|^2 + 2A|U_1|^2 + C|U_2|^2)U_3 + CU_1^*U_2^*U_4], \\ \frac{dU_4}{dt} &= E_{in} - (1 + i\eta\theta)U_4 + i\eta[(A|U_4|^2 + C|U_1|^2 + 2A|U_2|^2 + C|U_3|^2)U_4 + CU_2^*U_1^*U_3], \end{aligned} \quad (4)$$

Throughout the results and discussion section of our paper, including the numerical simulations of Eqs. (4), we used values of $A = 2/3$ and $C = 4/3$, since these correspond to those associated with silica glass fibers, where $\chi_{1122}^{(3)} \approx \chi_{1221}^{(3)} \approx \chi_{1212}^{(3)} \approx \chi_{1111}^{(3)}/3$.

Data availability

The data that support the plots within this paper and other findings of this study are available from the corresponding author upon reasonable request.

Code availability

The codes that support the plots within this paper and other findings of this study are available from the corresponding author upon reasonable request.

Received: 15 November 2022; Accepted: 28 July 2023;

Published online: 09 August 2023

References

- Bernstein, J. Spontaneous symmetry breaking, gauge theories, the higgs mechanism and all that. *Rev. Mod. Phys.* **46**, 7 (1974).
- Kazanas, D. Dynamics of the universe and spontaneous symmetry breaking. *Astrophys. J.* **241**, L59 (1980).
- Barbillon, G., Ivanov, A. & Sarychev, A. K. Applications of symmetry breaking in plasmonics. *Symmetry* **12**, 896 (2020).
- Bagheri, S., Mazzino, A. & Bottaro, A. Spontaneous symmetry breaking of a hinged flapping filament generates lift. *Phys. Rev. Lett.* **109**, 154502 (2012).
- Li, R. & Bowerman, B. Symmetry breaking in biology. *Cold Spring Harbor Perspect. Biol.* **2**, a003475 (2010).
- Kaplan, A. & Meystre, P. Enhancement of the sagnac effect due to nonlinearly induced nonreciprocity. *Optics Lett.* **6**, 590 (1981).
- Kaplan, A. & Meystre, P. Directionally asymmetrical bistability in a symmetrically pumped nonlinear ring interferometer. *Opt. Commun.* **40**, 229 (1982).
- Wright, E. M., Meystre, P., Firth, W. & Kaplan, A. Theory of the nonlinear sagnac effect in a fiber-optic gyroscope. *Phys. Rev. A* **32**, 2857 (1985).
- Woodley, M. T. et al. Universal symmetry-breaking dynamics for the kerr interaction of counterpropagating light in dielectric ring resonators. *Phys. Rev. A* **98**, 053863 (2018).
- Hill, L., Oppo, G.-L., Woodley, M. T. & Del'Haye, P. Effects of self-and cross-phase modulation on the spontaneous symmetry breaking of light in ring resonators. *Physical Review A* **101**, 013823 (2020).
- Woodley, M. T., Hill, L., Del Bino, L., Oppo, G.-L. & Del'Haye, P. Self-switching kerr oscillations of counterpropagating light in microresonators. *Phys. Rev. Lett.* **126**, 043901 (2021).
- Bitha, R. D., Giraldo, A., Broderick, N. G. & Krauskopf, B. Complex optical switching in a ring resonator with counter propagating light. In *Proc. Integrated Photonics Research, Silicon and Nanophotonics IF1A.3* (Optical Society of America, 2021).
- Cui, C., Zhang, L. & Fan, L. Control spontaneous symmetry breaking of photonic chirality with reconfigurable anomalous nonlinearity, arXiv preprint arXiv:2208.04866 (2022).
- Del Bino, L., Silver, J. M., Stebbings, S. L. & Del'Haye, P. Symmetry breaking of counter-propagating light in a nonlinear resonator. *Sci. Rep.* **7**, 1 (2017).
- Del Bino, L., Moroney, N. & Del'Haye, P. Optical memories and switching dynamics of counterpropagating light states in microresonators. *Opt. Express* **29**, 2193 (2021).
- Silver, J., Del Bino, L. & Del'Haye, P. A nonlinear enhanced microresonator gyroscope, in *CLEO: Science and Innovations. SM1M-2* (Optical Society of America, 2017).
- Cao, Q.-T. et al. Reconfigurable symmetry-broken laser in a symmetric microcavity. *Nat. Commun.* **11**, 1 (2020).
- Cao, Q.-T. et al. Experimental demonstration of spontaneous chirality in a nonlinear microresonator. *Phys. Rev. Lett.* **118**, 033901 (2017).
- Geddes, J., Moloney, J. V., Wright, E. M. & Firth, W. Polarisation patterns in a nonlinear cavity. *Opt. Commun.* **111**, 623 (1994).

20. Lugiato, L. A. & Lefever, R. Spatial dissipative structures in passive optical systems. *Phys. Rev. Lett.* **58**, 2209 (1987).
21. Haelterman, M., Trillo, S. & Wabnitz, S. Polarization multistability and instability in a nonlinear dispersive ring cavity. *JOSA B* **11**, 446 (1994).
22. Garbin, B. et al. Asymmetric balance in symmetry breaking. *Phys. Rev. Res.* **2**, 023244 (2020).
23. Moroney, N. et al. A Kerr polarization controller. *Nat. Commun.* **13**, 1 (2022).
24. Xu, G. et al. Spontaneous symmetry breaking of dissipative optical solitons in a two-component kerr resonator. *Nat. Commun.* **12**, 1 (2021).
25. Xu, G. et al. Breathing dynamics of symmetry-broken temporal cavity solitons in kerr ring resonators. *Opt. Lett.* **47**, 1486 (2022).
26. Ghosh, A., Hill, L., Oppo, G.-L. & Del'Haye, P. 4-field symmetry breakings in twin-resonator photonic isomers, arXiv preprint arXiv:2305.03583 (2023).
27. Del Bino, L. et al. Microresonator isolators and circulators based on the intrinsic nonreciprocity of the kerr effect. *Optica* **5**, 279 (2018).
28. Moroney, N. et al. Logic gates based on interaction of counterpropagating light in microresonators. *J. Lightw. Technol.* **38**, 1414 (2020).
29. Quinn, L. et al. Random number generation using spontaneous symmetry breaking in a kerr resonator. In *Proc. CLEO: QELS Fundamental Science* JTU3A-39 (Optica Publishing Group, 2022).
30. Biasi, S., Franchi, R., Bazzanella, D. & Pavesi, L. On the effect of the thermal cross-talk in a photonic feed-forward neural network based on silicon microresonators. *Front. Phys.* **10**, 1350 (2022).
31. Boyd, R. W., *Nonlinear Optics* (Academic press, 2020).
32. Pitois, S., Millot, G. & Wabnitz, S. Nonlinear polarization dynamics of counterpropagating waves in an isotropic optical fiber: theory and experiments. *JOSA B* **18**, 432 (2001).

Acknowledgements

L.H. acknowledges funding provided by the CNQO group within the Department of Physics at the University of Strathclyde, and the "Saltire Emerging Researcher" scheme through the Scottish University's Physics Alliance (SUPA) and provided by the Scottish Government and Scottish Funding Council. This work was further supported by the European Union's H2020 ERC Starting Grants 756966, the Marie Curie Innovative Training Network "Microcombs" 812818 and the Max Planck Society.

Author contributions

G.L.O., P.D.H. and L.H. defined the research project. L.H. completed the derivation of the used model and performed its numerical analysis. L.H. wrote the manuscript with input from G.L.O. & P.D.H.

Funding

Open Access funding enabled and organized by Projekt DEAL.

Competing interests

The authors declare no competing interests.

Additional information

Supplementary information The online version contains supplementary material available at <https://doi.org/10.1038/s42005-023-01329-3>.

Correspondence and requests for materials should be addressed to Lewis Hill.

Peer review information *Communications Physics* thanks Avik Dutt and the other anonymous reviewers for their contribution to the peer review of this work. A peer review file is available.

Reprints and permission information is available at <http://www.nature.com/reprints>

Publisher's note Springer Nature remains neutral with regard to jurisdictional claims in published maps and institutional affiliations.



Open Access This article is licensed under a Creative Commons Attribution 4.0 International License, which permits use, sharing, adaptation, distribution and reproduction in any medium or format, as long as you give appropriate credit to the original author(s) and the source, provide a link to the Creative Commons licence, and indicate if changes were made. The images or other third party material in this article are included in the article's Creative Commons licence, unless indicated otherwise in a credit line to the material. If material is not included in the article's Creative Commons licence and your intended use is not permitted by statutory regulation or exceeds the permitted use, you will need to obtain permission directly from the copyright holder. To view a copy of this licence, visit <http://creativecommons.org/licenses/by/4.0/>.

© The Author(s) 2023